AIAA 94-0100

Nonequilibrium Structure of H_2-Air Combustion in Turbulent Jets

Eric S. Bish and Werner J.A. Dahm

Department of Aerospace Engineering
The University of Michigan
Ann Arbor, MI

32nd Aerospace Sciences Meeting & Exhibit

January 10-13, 1994 / Reno, NV

Nonequilibrium Structure of H_2-Air Combustion in Turbulent Jets

Eric S. Bish[1] and Werner J.A. Dahm[2]

Gas Dynamics Laboratories, Department of Aerospace Engineering
The University of Michigan, Ann Arbor, MI 48109-2140

Results are presented for chemical species and temperature fields for nonpremixed turbulent jet flames of hydrogen in air. The analyses are based on a strained dissipation and reaction layer formulation of nonequilibrium chemistry in turbulent reacting flows, relating the chemical state to the mixing state of a conserved scalar by the underlying turbulent flow. This physically-based formulation results from observations that the instantaneous scalar energy dissipation rate field in turbulent mixing is essentially confined to locally one-dimensional strained dissipation layers. These scalar dissipation layers are independent of the chemical state of the flow and are instead a direct consequence of the dynamics of scalar mixing at large Peclet (*ReSc*) numbers. The locally one-dimensional dissipation layers allow a one-dimensional formulation for the underlying chemical species fields. The resulting strained dissipation and reaction layer model has similarities with the classical "flamelet" model but is based on entirely different physical observations, derived from entirely different arguments, and limited by an entirely different and more widely applicable set of conditions. Moreover, the formulation involves boundary conditions for the local chemical state that differ fundamentally from those used in flamelet models. Results obtained for chemical species fields accessible to conventional PLIF diagnostics demonstrate remarkable resemblances to direct imaging measurements over conditions ranging from near equilibrium to deep nonequilibrium, showing the predominance of thin (flamelet) regions under conditions of relatively weak chemical nonequilibrium and the natural emergence and dominance of broad (distributed) zones for increasing nonequilibrium. Temperature fields also display behavior observed experimentally. Because the above formulation allows for species concentration and temperature calculations to be made for arbitrarily large equilibrium departures, for the moderate and deep nonequilibrium cases subequilibrium temperature values as well as sub and superequilibrium OH values are observed.

1. Introduction. Results from detailed conserved scalar imaging measurements in nonreacting turbulent flows [1-6] as well as direct numerical simulations (DNS) of passive scalar mixing in turbulent flows [7-11] have shown that, whereas the underlying hydrodynamics of turbulent flows are quite complex, the structure of scalar mixing in such flows is considerably simpler. For dynamically passive conserved scalar fields $\zeta(\mathbf{x},t)$ with Schmidt numbers (ν/D_ζ) of unity or larger, essentially all of the instantaneous scalar energy dissipation rate field $\chi(\mathbf{x},t) \equiv (ReSc)^{-1}\nabla\zeta\cdot\nabla\zeta(\mathbf{x},t)$ is organized into locally one-dimensional layer-like dissipation sheets. Examples of these dissipation layers can be seen in Fig. 1 from Buch & Dahm [4]. These scalar dissipation layers are a consequence solely of the hydrodynamics of scalar mixing in turbulent flows. The dynamics of the strain-diffusion competition involved in scalar mixing at large Peclet (*ReSc*) numbers that leads to

1 AIAA Member
2 Associate Professor, AIAA Member

the inexorable formation of such layer-like scalar dissipation structures is discussed in detail in Ref. [4]. In reacting turbulent flows, the advection-diffusion balance that leads to the formation of these ubiquitous scalar dissipation layers is present as well. In the presence of combustion heat release the individual chemical species diffusivities D_i vary with local temperature, however; the hydrodynamic viscosity ν scales in essentially the same way and thus Sc remains essentially constant near unity. This leads to a change in the lengthscale characterizing the thickness of these layer-like dissipation structures but does not alter the basic strain-diffusion competition that establishes these structures. Moreover, for heat release values typical of hydrocarbon combustion, the local velocity gradients leading to formation and preservation of these dissipation sheets should remain dominant in turbulent flows with combustion as well. Recent results from scalar imaging measurements by Long [12] as well as DNS computations appear to confirm that these layer-like scalar dissipation structures remain present even in turbulent flows undergoing highly exothermic combustion reactions.

The implications of this fundamentally layer-like structure of scalar mixing in turbulent flows are substantial, especially for turbulent combustion. As noted above, these dissipation layers result entirely for hydrodynamical reasons. Thus *all* conserved scalar quantities with $Sc \geq 1$ must have their scalar energy dissipation concentrated in such locally one-dimensional layer-like structures. This will be true regardless of whether the scalar is a passive physical quantity (such as an inert dye or gaseous tracer) or a more abstract quantity formed from the concentrations of various chemical species evolving in a chemically reacting flow (such as any of various mixture fraction variables). Thus the dissipation fields associated with all conserved scalar mixture fractions must *also* remain manifestly layer-like irrespective of the degree of chemical nonequilibrium to which the various constituent chemical species fields are subjected - the presence of locally one-dimensional dissipation layers in mixture fraction fields is entirely independent of the chemical state in the flow. As a consequence, any model relating the combustion chemistry in a turbulent flow to the underlying fluid dynamics must, at a minimum, recover this layer-like dissipation structure once the resulting reactive species concentrations are formed into mixture fraction variables. Conversely, the inherently layer-like structure of the dissipation rate fields associated with mixture fraction variables in turbulent flows provides a rigorous starting point for models of nonequilibrium chemistry in turbulent flows.

Such a model for nonequilibrium combustion chemistry in turbulent flows was recently proposed [13]. In this paper, we outline this strained dissipation and reaction layer formulation for turbulent reacting flows and then use it to examine certain features related to the structure of hydrogen-air jet diffusion flames. In particular, we construct the OH radical and temperature fields at three differing levels of chemical nonequilibrium and relate these to recent imaging measurements. The paper is organized as follows. In §2 we review the strained dissipation and reaction layer formulation. Following this, §3 explains its application to conserved scalar imaging measurements in a turbulent jet, and §4 presents results for OH concentration and temperature fields in three different hydrogen-air jet diffusion flames. Conclusions are drawn in §5.

2. The Strained Dissipation and Reaction Layer Formulation.

The ubiquitous scalar energy dissipation layers noted above allow for a physically-based formulation that relates the mixing state of a conserved scalar by the underlying turbulent flow to the chemical state of nonequilibrium combustion occurring within the flow. This approach begins by noting that any conserved scalar mixture fraction variable ζ_i can be written as a linear sum over the chemical species fields $Y_j(\mathbf{x},t)$ as

$$\zeta_i(\mathbf{x},t) = \sum_{j=1}^{N} a_{i,j} Y_j(\mathbf{x},t) \qquad i = 1,2,\ldots,m \qquad (1)$$

where N is the number of chemical species, m the number of elements involved in the chemical system, and $a_{i,j} \geq 0$. As is typically the case in conserved scalar formulations, we have for the moment assumed the diffusivities of all species to be the same. Owing to the locally one-dimensional state of the scalar field within any given dissipation layer, derivatives of ζ_i along the local layer-normal coordinate n typically far exceed those along the layer. Thus each of the conserved scalar transport

equations reduces to the locally one-dimensional (parabolized) form

$$\frac{\partial \zeta_i}{\partial t} - \varepsilon(t) n \frac{\partial \zeta_i}{\partial n} - \frac{1}{\rho}\frac{\partial}{\partial n}\left(\rho D \frac{\partial \zeta_i}{\partial n}\right) = 0 \qquad (2)$$

where $\varepsilon(t)$ is the local time-varying strain rate along the layer-normal direction resulting from the local linear expansion of the velocity field $\mathbf{u}(\mathbf{x},t)$. As is evident in Fig. 1, in general the scalar dissipation layers in turbulent flows do not involve pure fuel or pure air on either side of the layer. Instead the correct *local* boundary conditions for (2) can be expressed as

$$\zeta_i \to \zeta_i^{\pm} \quad as \quad n \to \pm\infty \qquad (3)$$

where the appropriate $\zeta_i^{\pm}$ typically vary slowly along the layer.

Replacing ζ_i in (2) with its definition in terms of the various chemical species concentration fields in (1) and recalling that the $a_{i,j}$ are constants gives

$$\begin{pmatrix} a_{1,1} & a_{1,2} & \cdots & a_{1,N} \\ a_{2,1} & a_{2,2} & \cdots & a_{2,N} \\ \vdots & \vdots & \ddots & \vdots \\ a_{m,1} & a_{m,2} & \cdots & a_{m,N} \end{pmatrix} \begin{pmatrix} L\left[Y_1(\mathbf{x},t)\right] \\ L\left[Y_2(\mathbf{x},t)\right] \\ \vdots \\ L\left[Y_N(\mathbf{x},t)\right] \end{pmatrix} = \begin{pmatrix} 0 \\ 0 \\ \vdots \\ 0 \end{pmatrix} \qquad (4)$$

where

$$L\left[Y_j(\mathbf{x},t)\right] \equiv \left[\frac{\partial Y_j}{\partial t} - \varepsilon(t) n \frac{\partial Y_j}{\partial n} - \frac{1}{\rho}\frac{\partial}{\partial n}\left(\rho D \frac{\partial Y_j}{\partial n}\right) - w_j/\rho\right] \qquad (5)$$

Here we have also introduced the requirement that, since the ζ_i are conserved, the weighted chemical species reaction rate terms $w_j(\mathbf{x},t)$ must sum to zero as

$$\sum_{j=1}^{N} a_{i,j}\, w_j(\mathbf{x},t) \equiv 0 . \qquad (6)$$

We now want to consider the implications of (4) - (6) for the structure of the $Y_j(\mathbf{x},t)$ fields. We argue that these constraints together require that the only physically realizable solution is the trivial case $L[Y_j(\mathbf{x},t)] \equiv 0$, in which case the species conservation equations satisfy locally one-dimensional advection-diffusion-reaction equations within each dissipation layer. There are three key physical requirements that we argue demand this trivial solution in (4).

(i) In (4) all the $a_{i,j} \geq 0$ since from (1) each mixture fraction ζ_i is simply a sum over all the chemical species Y_j of their contributions to the tally of each element i. Thus, owing to the fact that all the $a_{i,j}$'s have the same sign, the zero sums in (4) can only result from either the trivial solution $L[Y_j(\mathbf{x},t)] \equiv 0$ or else from a fortuitous cancellation of positive and negative $L[Y_j(\mathbf{x},t)]$'s. If the latter is the case then this cancellation would need to be preserved for each of the m sums corresponding to the elements $i = 1, 2, \ldots, m$ for the single set of species fields $Y_j(\mathbf{x},t)$. That is to say, the single set of $Y_j(\mathbf{x},t)$ fields needs to satisfy m simultaneous zero sums.

(ii) Since typically $N \gg m$, there are combinations of the $L[Y_j(\mathbf{x},t)]$'s that will produce these m zero sums in *(i)* above, however each of these combinations imposes specific relations between the various $Y_j(\mathbf{x},t)$ fields. The restricted $Y_j(\mathbf{x},t)$ fields necessary to preserve these m zero sums would, at the same time, need to be consistent with the kinetics associated with the resulting elementary reaction rate terms. In other words, each of the combinations of the $Y_j(\mathbf{x},t)$ fields that satisfies the required cancellation of $L[Y_j(\mathbf{x},t)]$'s in *(i)* corresponds to a set of net elementary reaction rates $w_j(\mathbf{x},t)$. However the resulting $w_j(\mathbf{x},t)$ fields must at the same time preserve the zero sum in (6). This would, at a minimum, greatly reduce the set of $L[Y_j(\mathbf{x},t)]$'s simultaneously consistent with both (4) and (6).

(iii) Lastly, the zero sums in (4) and (6) must be preserved for *all* possible chemical systems, not merely any particular reaction set under consideration. No features of the reaction kinetics specific to any one chemical system can be invoked to satisfy the relations among the $Y_j(\mathbf{x},t)$ fields necessary to achieve cancellation of positive and negative $L[Y_j(\mathbf{x},t)]$'s in *(i)* while at the same time preserving the additional zero sum over the

weighted $w_j(\mathbf{x},t)$'s in *(ii)* for the resulting elementary reaction rates. In other words, the layer-like structure in the scalar dissipation field as expressed by (4) - (6) must be recovered for *every conceivable* elementary chemical system that could hypothetically occur.

Each one of these three observations places strong constraints on the $Y_j(\mathbf{x},t)$ fields. The fact that all three of these requirements must be simultaneously met by the coupled $Y_j(\mathbf{x},t)$ fields suggests a set of constraints collectively so restrictive as to be physically unrealizable. We therefore hypothesize that the set of simultaneous conditions under which (4) can have a non-trivial solution are mutually exclusive and that the only physically realizable solution is the trivial case $L[Y_j(\mathbf{x},t)] \equiv 0$ for each j, namely

$$\frac{\partial Y_j}{\partial t} - \varepsilon(t) n \frac{\partial Y_j}{\partial n} - \frac{1}{\rho}\frac{\partial}{\partial n}\left(\rho D \frac{\partial Y_j}{\partial n}\right) = w_j/\rho . \qquad (7)$$

In other words, the one-dimensionality of the local conserved scalar field across each of these strained dissipation layers implies a locally one-dimensional structure for the underlying chemical species fields within the layer. However, owing to the *local* boundary conditions on (7), this does *not* imply that the resulting $Y_j(\mathbf{x},t)$ fields must be layer-like, as will be seen from the results.

As noted in (3), these locally one-dimensional strained dissipation and reaction layers are in general not between pure fuel and air. Instead, the appropriate local boundary conditions on (7) are

$$Y_j \to Y_j^{\pm} \quad as \quad n \to \pm\infty . \qquad (8)$$

It is appropriate at this point to comment on the similarities and differences between the present strained dissipation and reaction layer (SDRL) model and the classical flamelet model, since both arrive at the same governing equations. The SDRL formulation above is a consequence of the one-dimensionality of any conserved scalar variable across the locally layer-like structures seen to dominate scalar energy dissipation rate fields in turbulent flows. The formulation, in this sense, is based entirely on hydrodynamical arguments and makes no statements about thinness of reaction zones or places any other requirements on the reaction chemistry. In effect, we are arguing precisely the opposite point of view from that usually taken in deriving the classical "flamelet" model [14]. In deriving the flamelet model, conditions are assumed for which the flamelet is thin, and the species transport equations then formally reduce to locally one-dimensional equations which in turn dictate a locally one-dimensional structure in the mixture fraction fields $\zeta_i(\mathbf{x},t)$. However, the conditions under which the requisite thin flamelet assumption actually holds are so restrictive as to render the resulting classical flamelet model useful only for small equilibrium departures. Here we take the exact opposite point of view. We *begin* with the physical observation that the mixture fraction fields $\zeta_i(\mathbf{x},t)$ in turbulent flows must be locally one-dimensional and then argue that this requires the constituent chemical species fields $Y_j(\mathbf{x},t)$ to also be one-dimensional. The thinness requirement is expressed in various flamelet implementations either as a requirement that variations in the scalar dissipation within the reaction zone must be negligible [14-16] or else that these variations can be modeled via some presumed function such as $\chi \sim \zeta^p$ [17] or the self-similar solution of the scalar transport equation (2) for free stream boundary conditions [18].

The latter class of flamelet models is most closely related to the present approach, though the thinness requirement to which these are subject is not a constraint here. Moreover the appropriate *local* boundary conditions in (8) for the one-dimensional advection-diffusion-reaction equations within any given dissipation layer differ fundamentally from classical flamelet models. Instead, these correspond to the mass fraction values $Y_j^{\pm}$ between neighboring dissipation layers. In practice, the information required to specify the correct $Y_j^{\pm}$ will rarely be available. However, the physical nature of the approach developed here allows some insight into how these boundary conditions may be simplified. In particular, we note that the mapping from (ζ,χ) to the strain rate ε, where

$$\varepsilon = 2\pi D\left[\frac{\nabla\zeta\cdot\nabla\zeta}{(\zeta^+-\zeta^-)^2}\right] exp\, 2\left\{ erf^{-1}\left[\frac{\zeta - \frac{1}{2}(\zeta^+ + \zeta^-)}{\frac{1}{2}(\zeta^+ - \zeta^-)}\right]\right\}^2 \cdot f(\zeta) \qquad (9)$$

is very sensitive to the conserved scalar boundary values

ζ^+ and ζ^- in (3). Since the strain rate drives the local molecular mixing rate and thus plays a dominant role in setting the depth of nonequilibrium chemistry, it is of primary importance to account for the scalar boundary values properly. In comparison with ζ^+ and ζ^-, the corresponding chemical species boundary values Y_j^+ and Y_j^- would appear to have less of an effect on the nonequilibrium levels within the layer since these influence the reaction progress only indirectly. The local departures from chemical equilibrium in each of the species concentrations may therefore be determined principally by the local scalar value ζ and the *correct* local strain rate $\varepsilon(\zeta, \chi; \zeta^+, \zeta^-)$. A direct test of this hypothesis for simplifying the local boundary conditions must await results of a numerical study currently underway.

3. Application to Turbulent Jet Flames. We have applied this strained dissipation and reaction layer formulation to examine variations in the structure of hydroxyl radical concentration and temperature fields for increasing degrees of chemical nonequilibrium in a turbulent jet diffusion flame. The results obtained are based on imaging measurements of conserved scalar fields obtained in the corresponding nonreacting flow. The experimental technique has been described in detail elsewhere [4-6]. Briefly, these conserved scalar imaging measurements were made in the self-similar far field of an axisymmetric coflowing turbulent jet in the Turbulent Diffusion Flame (TDF) wind tunnel at the Combustion Research Facility of Sandia National Laboratories. The flow was established in the 30 cm × 30 cm × 200 cm test section of the forced draft vertical tunnel with free stream velocity U_∞ by issuing a jet of undiluted technical grade propane with momentum flux J_o through a 7.7 mm diameter nozzle. The beam from a 300 mJ/pulse Nd:YAG laser was doubled to 532 nm and formed into a thin sheet passing through the flow. The $1/e$ laser sheet thickness was measured as 230 μm. Rayleigh scattered light from this sheet was imaged onto a 14-bit, slow-scanned, cooled, nonintensified imaging array. The array was sampled in a 256 × 512 × 8-bit format, with each element measuring 23 μm × 23 μm. The imaging optics were arranged to give a 1:1 image ratio with the array output giving the Rayleigh signal integrated over the 10 ns laser pulse duration. The measurement location was centered 39 nozzle diameters downstream of the jet exit at a local outer-scale Reynolds number $Re \approx 14{,}000$. The spatial and temporal resolution achieved were sufficient to distinguish the smallest spatial and temporal scales in the scalar field. Reference measurements with pure air in the test section gave the laser sheet intensity distribution and allowed the effects of non-uniformities in the laser sheet to be largely removed from the data. The Rayleigh signal at each point was then converted to the instantaneous value of the propane mass fraction, yielding a *generic* $Sc \approx 1$ conserved scalar field $\zeta(\mathbf{x},t)$ in the turbulent flow. The structure of the scalar energy dissipation rate field $\nabla\zeta\cdot\nabla\zeta(\mathbf{x},t)$ was obtained from the measured $\zeta(\mathbf{x},t)$ data using linear central differences on a 3 × 3 template centered on each data point.

Figure 1 (top) shows a typical 256 × 512 data plane of the instantaneous conserved scalar field $\zeta(\mathbf{x},t)$. The 256 different colors denote ranges of conserved scalar values as indicated, with pure blue beginning at $\zeta(\mathbf{x},t) = 0$ corresponding to pure air and increasing uniformly to pure red denoting the highest conserved scalar values in the data. The jet centerline runs down the right edge of the plane, and the axes indicate the spatial extent in terms of the local strain-limited scalar gradient lengthscale λ_D. Derivatives of the measured conserved scalar field give the projection of the true three-dimensional scalar gradient vector $\nabla\zeta(\mathbf{x},t)$ into the plane. Figure 1 (bottom) shows the logarithm of the corresponding scalar dissipatio rate

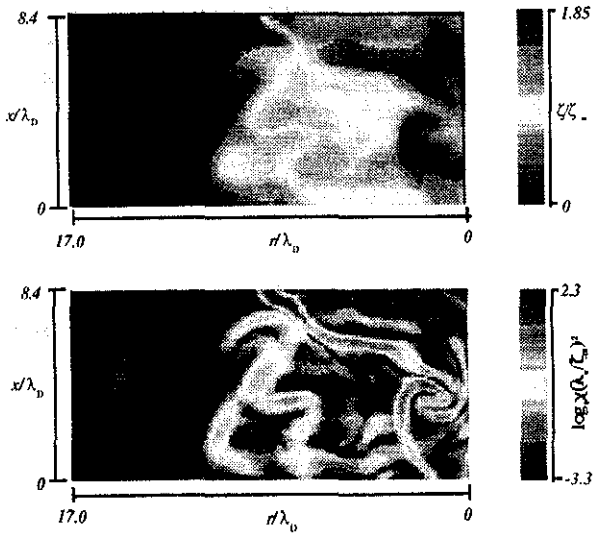

Fig. 1. Scalar mixing measurements for a $Sc \approx 1$ conserved scalar field. The conserved scalar field $\zeta(\mathbf{x},t)$ (top). The associated two-dimensional scalar dissipation rate field $log_e \chi(\mathbf{x},t)$ (bottom).

field formed from this projection, $log_e \nabla\zeta \cdot \nabla\zeta(\mathbf{x},t)$. The 256 different colors denote the local scalar dissipation rate with black beginning at $\nabla\zeta \cdot \nabla\zeta = 0$ and pure blue through pure red denoting logarithmically increasing dissipation rates.

The local outer variables $u(x)$ and $\delta(x)$ and the mass fraction-based conserved scalar field $\zeta(\mathbf{x},t)$ follow self-similar scalings with downstream location x in the far field of axisymmetric turbulent jets. Since these scalings produce a Reynolds number that remains constant with increasing downstream distance, measurements such as those in Fig. 1 can be rescaled to map the instantaneous scalar and dissipation rate fields to any x-location in the self-similar far field of the flow. A given set of chemical reactions occurring in this conserved scalar field would then correspond to a turbulent jet diffusion flame of length L, where the flame tip is taken to occur at the x-location for which the maximum conserved scalar value achieves stoichiometry for the hydrogen-air chemical system being considered. Chemical species concentration and temperature fields can then be constructed from the local values of the scalar and dissipation rate fields using the steady strained dissipation and reaction layer formulation with a library for hydrogen-air chemistry generated from the Sandia one-dimensional, axisymmetric, opposed flow diffusion flame code.

The SDRL formulation as implemented here addresses the reaction dynamics in terms of a *single* conserved scalar. This necessarily precludes any consideration of preferential diffusion effects among the chemical species present in the flow. Even though we are limited by the governing conservation equations to a single diffusivity in describing the scalar mixing, numerical calculations of the chemical composition and thermodynamic properties across any layer within the flame allow for differential diffusion as well as nonunity Lewis number effects to be addressed. To examine these effects one-dimensional, axisymmetric, opposed flow flame calculations were performed for H_2-Air chemistry at a strain rate $\varepsilon = 7300$ /s for three different cases: (A) mixture averaged species diffusivities with $Le = 1$, (B) multicomponent species diffusivities with $Le \neq 1$, and (C) multicomponent species diffusivities with $Le = 1$. Fig. 2 (top) shows the conserved scalar profiles across the layer for each of the three cases and demonstrates its near

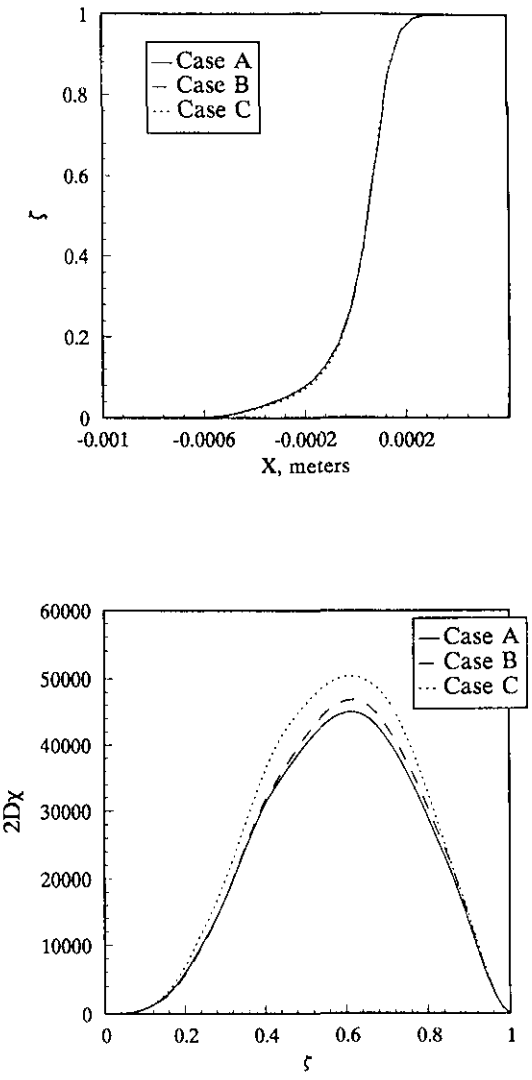

Case A: mixture averaged species diffusivities with Lewis number = 1.

Case B: multicomponent species diffusivities with Lewis number ≠ 1.

Case C: multicomponent species diffusivities with Lewis number = 1.

Fig. 2 (top) Conserved scalar profiles (bottom) scalar energy dissipation rate profiles for H_2-Air one-dimensional opposed flow diffusion flame, $\varepsilon = 7300$ /s.

invariance to differing species transport definitions. Despite this fact the corresponding one-dimensional scalar energy dissipation rate, $2D(\partial\zeta/\partial x)^2$, profiles shown in Fig. 2 (bottom) display considerable magnitude differences. Variations in magnitude can be seen for other properties across the layer as well. Fig. 3 shows the differing OH mass fraction, temperature, and H_2O mass fraction profiles for the three cases. Whereas the temperature profiles show very small responses to changes in the preferential diffusion and Lewis number variations, the OH and H_2O mass fraction profiles display substantial differences. The largest disparities occur near stoichiometry for OH and across nearly the entire layer for H_2O. Note that for H_2O only the cases using multicomponent species diffusivities yield profiles that match the equilibrium profile as would be expected since H_2O remains essentially in equilibrium. Thus we find that even though the SDRL model is a single conserved scalar formulation, the use of multicomponent species diffusivities and nonunity Lewis number is very important in providing accurate numerical calculations for the chemical and thermodynamic properties across the layer.

To vary the global Damköhler number while holding the Reynolds number fixed, the effective nozzle diameter and exit velocity are changed as shown in Fig. 4. With a characteristic temperature of roughly 1800 K and with $\nu \sim T^{1.5}$, a cold-flow Reynolds number of 210,000 in Fig. 4 produces a hot-flow conserved scalar field consistent with the Re = 14,000 measurements in Fig. 1. Figure 4 also shows the conditions for each of the three cases for which results are presented below. These correspond to conditions in the flame ranging from near equilibrium (Case 1) to moderate nonequilibrium (Case 2) to deep nonequilibrium (Case 3). All results presented below are constructed via the SDRL formulation outlined in §2 using the conserved scalar and scalar dissipation fields in Fig. 1 with a uniform rescaling of these ζ and χ fields mapping them to any x/L location for any of the three cases considered. Relative local strain rates for each of the three cases and each of the four downstream locations are given in Table 1.

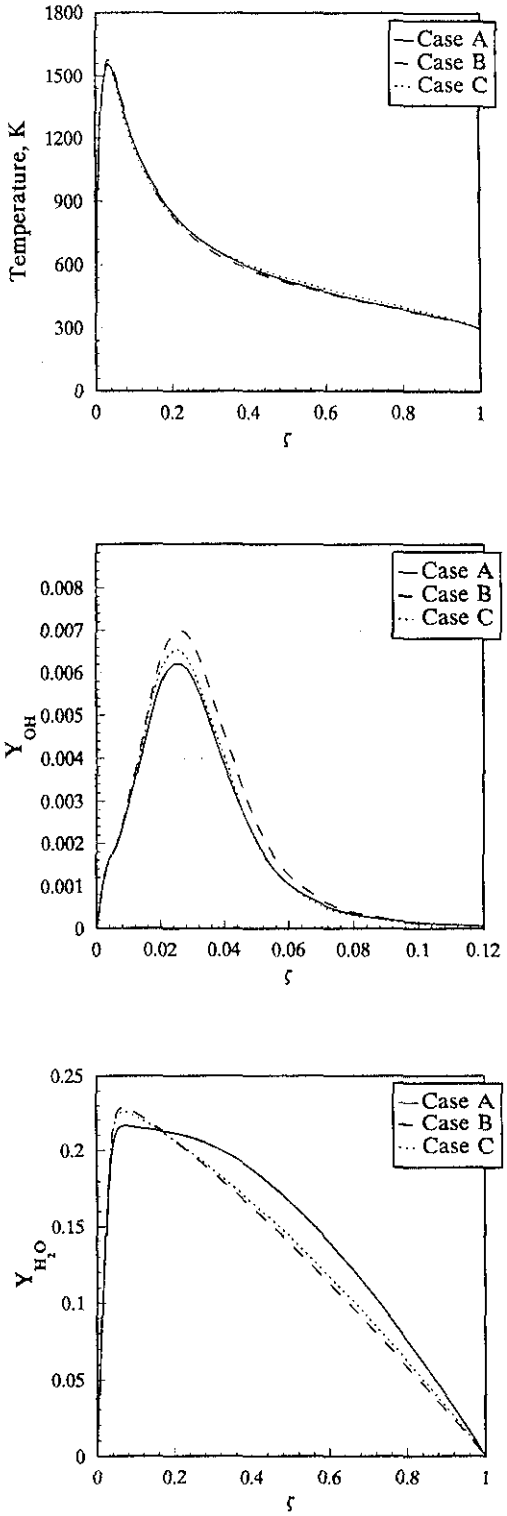

Fig. 3. Temperature (top), Y_{OH} (middle), and Y_{H2O} (bottom) profiles for H_2-Air one-dimensional opposed flow diffusion flame, ε = 7300 /s , for the cases described in Fig. 2.

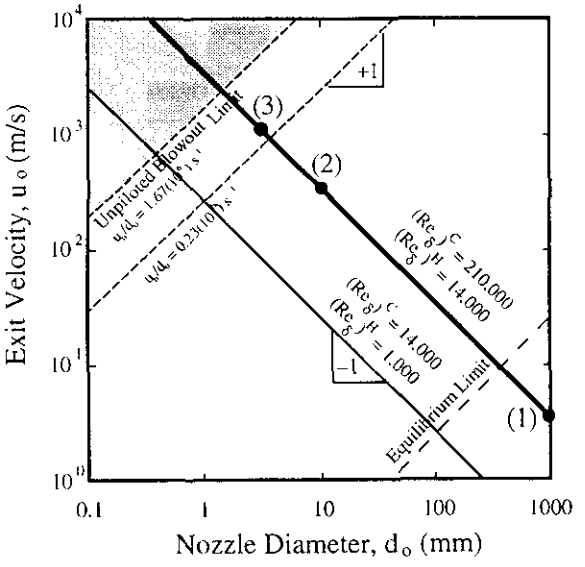

Fig. 4. Map of source conditions for turbulent *hydrogen-air jet diffusion flames, showing depth of* chemical nonequilibrium relative to the unpiloted blowout limit, given by $u_o/d_o = 1.67 \cdot 10^6\ s^{-1}$. Solid line denotes conditions giving far-field hot flow Reynolds number $Re_\delta = 14{,}000$ corresponding to cold flow $Re_\delta = 210{,}000$. Dashed lines denote constant global Damköhler number (u_o/d_o = const.) Shown are the conditions for three cases, giving (Case 1) the equilibrium limit, (Case 2) moderate nonequilibrium, and (Case 3) deep nonequilibrium.

x/L	Case 1	Case 2	Case 3
0.25	10 (10^{-5})	1	10
0.50	2.5 (10^{-5})	0.25	2.5
0.75	1.1 (10^{-5})	0.11	1.1
1.00	0.6 (10^{-5})	0.06	0.6

Table 1. Relative strain rates at each of the four downstream locations and three cases identified in Fig. 4.

4. Results. Figs. 5-7 and 9-11 show the resulting OH mass fraction $Y_{OH}(\mathbf{x},t)$ and temperature $T(\mathbf{x},t)$ fields obtained from the SDRL formulation throughout the entire length of the flame for each of the three cases in Fig. 4. In each case the fields are shown at four different downstream locations relative to the mean flame length L centered at x/L = 0.25, 0.50, 0.75 and 1.0. The size of each panel has been correctly scaled and placed for its downstream location to give a proper indication of the structure of the flame. Differences evident in the fields when comparing panels at the same downstream location for the three cases shown are due solely to the differing degrees of nonequilibrium. However, changes among panels corresponding to differing x/L values for the same case reflect changes in both the depth of nonequilibrium as well as changes in the scalar and dissipation rate values with increasing downstream location in the flame. For the jet similarity scalings, the scalar field values decrease with increasing distance from the jet source as $\zeta \sim x^{-1}$. Coupled with the linear increase in all length scales in the jet with increasing x, the resulting scalar dissipation field values decrease with distance from the jet source like $\nabla\zeta \cdot \nabla\zeta \sim x^{-4}$. Thus, in examining these results it must be kept in mind that comparisons made among different cases but at the same x/L location show the effects of the degree of nonequilibrium only while comparisons made at different downstream locations within the same case demonstrate the effects of both nonequilibrium level and changes in the scalar field values. Arranging the results as shown allows separating the changes resulting solely from the degree of nonequilibrium from those resulting from changes in the conserved scalar and dissipation rate values.

In Figs. 5-7 we examine the temperature fields $T(\mathbf{x},t)$ that result from the SDRL formulation for each of the three cases considered. Note the transition in the maximum radial temperature location from near the jet edge far upstream to the centerline for increasing x/L locations. The maximum radial temperatures initially increase with increasing downstream location then begin to decrease in value as the flame tip is approached. Centerline temperature values display this same behavior. The trends exhibited by these fields for each of the three cases considered are consistent with experimental measurements in flames under similar combustion conditions [19,20,21]. Figs. 5-7 also show the associated scatter plots for the temperatures obtained. These more clearly show the range of temperature values computed within the flame. For the near equilibrium case the SDRL

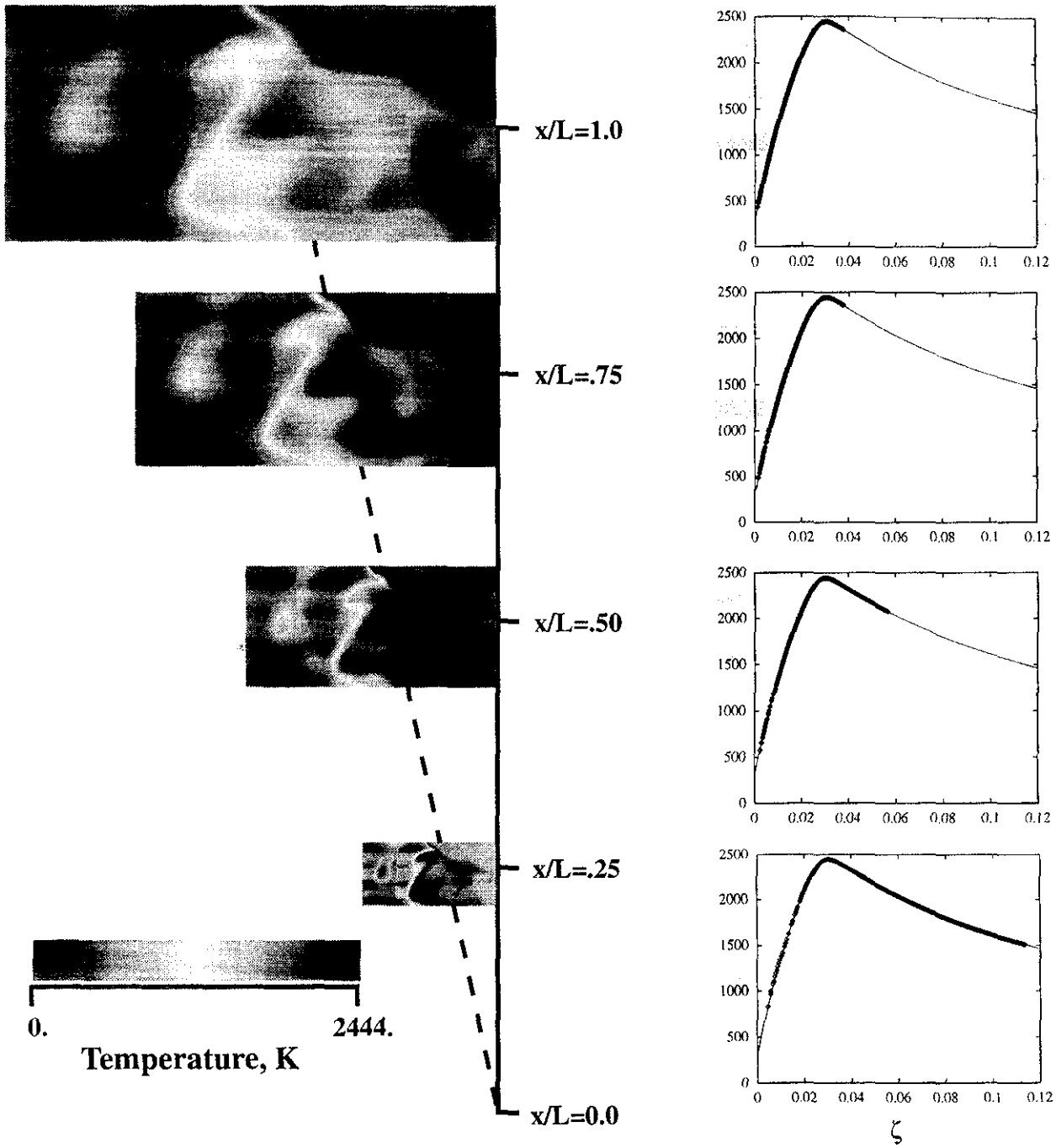

Fig. 5. Strained diffusion and reaction layer (SDRL) model results for composite temperature fields $T(\mathbf{x},t)$ and the associated scatter plots for a hydrogen-air turbulent jet diffusion flame in the equilibrium limit (Case 1) at four downstream locations: x/L = 0.25, 0.50, 0.75, and 1.0. Compare with Figs. 6 and 7 to see the effect of varying Damköhler number. The solid curve in each of the scatter plots gives the adiabatic, equilibrium temperature distribution.

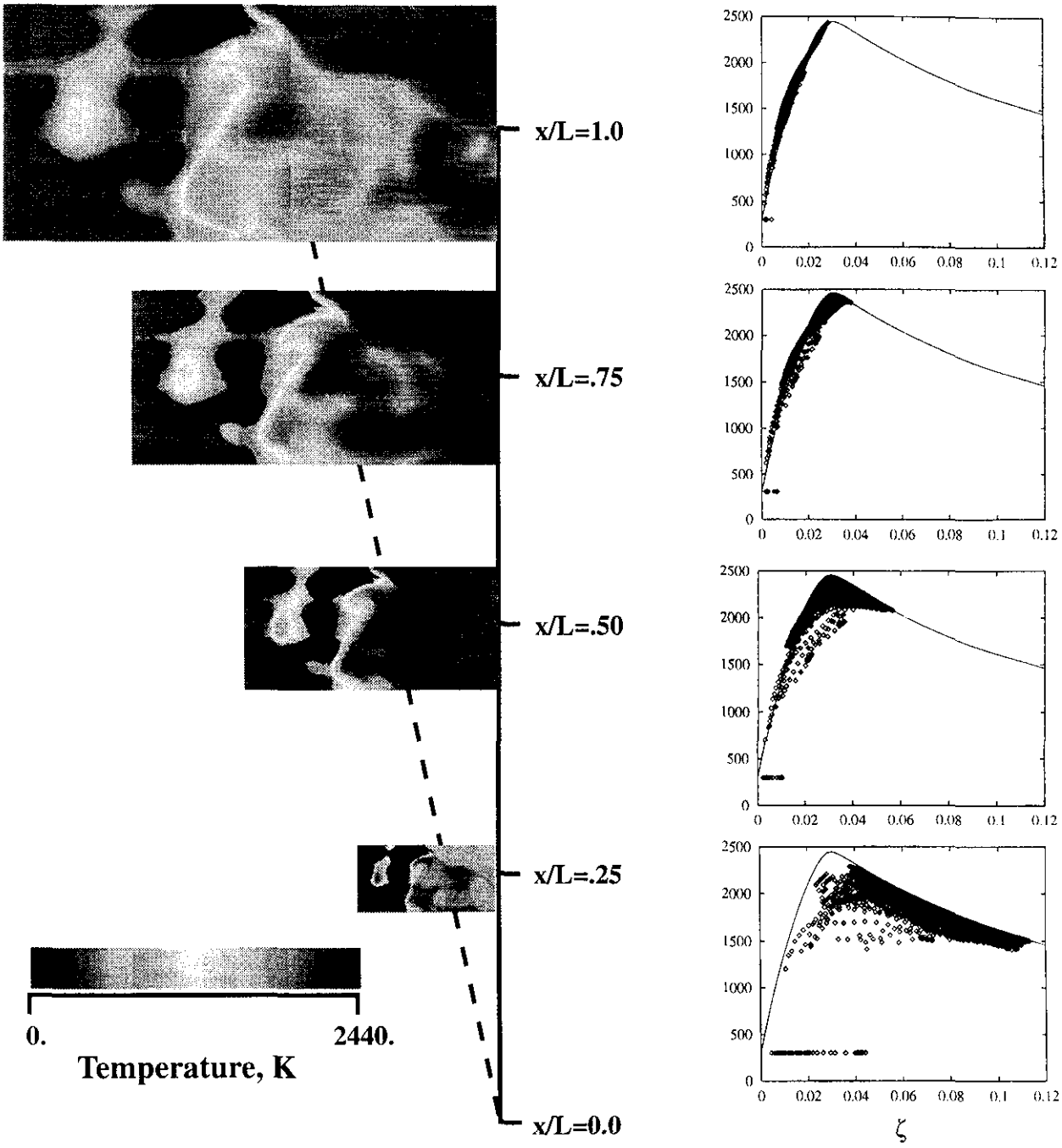

Fig. 6. Strained diffusion and reaction layer (SDRL) model results for composite temperature fields $T(\mathbf{x},t)$ and the associated scatter plots for a hydrogen-air turbulent jet diffusion flame at moderate nonequilibrium (Case 2) conditions at four downstream locations: x/L = 0.25, 0.50, 0.75, and 1.0. Compare with Figs. 5 and 7 to see the effect of varying Damköhler number. The solid curve in each of the scatter plots gives the adiabatic, equilibrium temperature distribution.

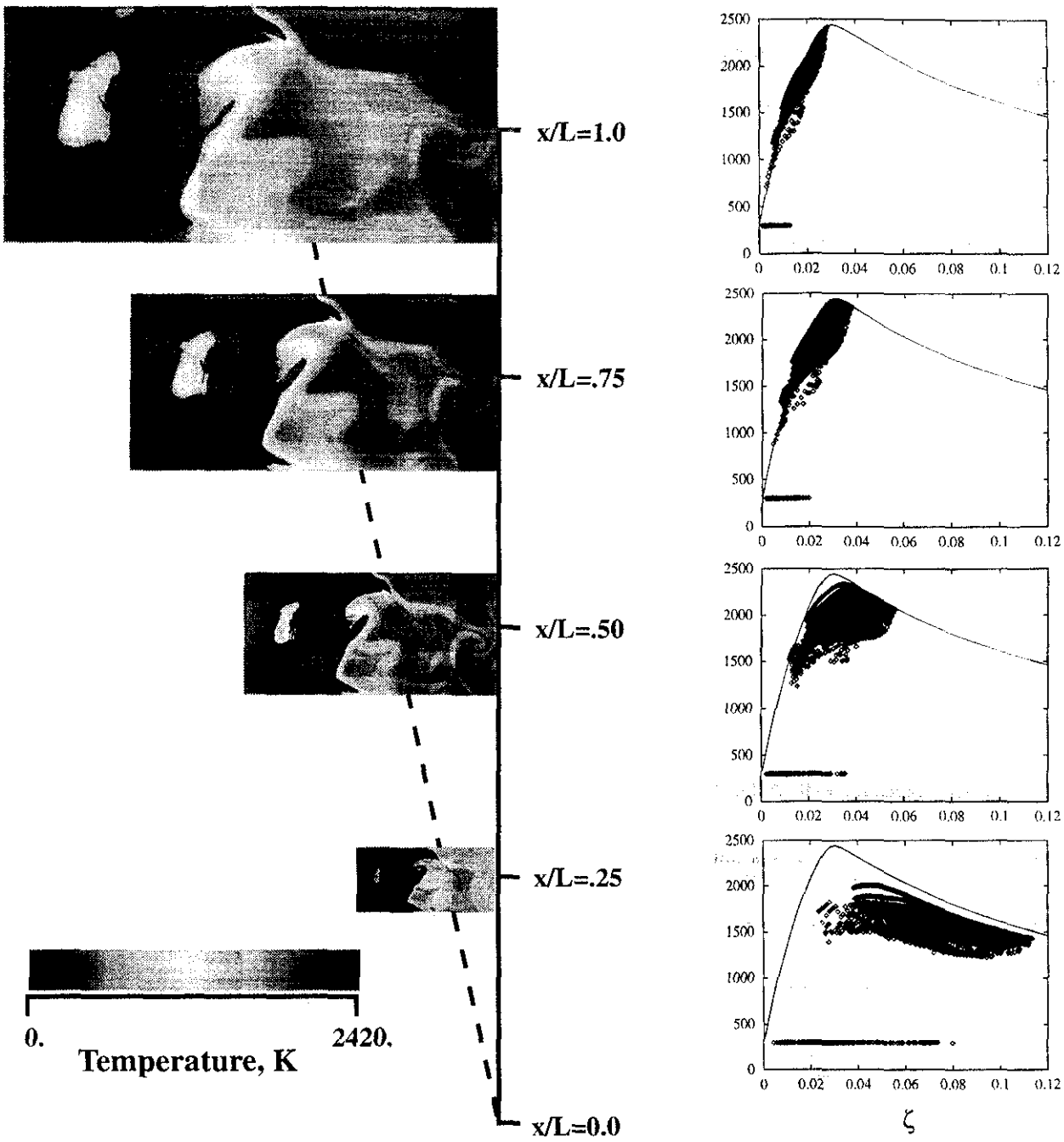

Fig. 7. Strained diffusion and reaction layer (SDRL) model results for composite temperature fields $T(\mathbf{x},t)$ and the associated scatter plots for a hydrogen-air turbulent jet diffusion flame at deep nonequilibrium (Case 3) conditions at four downstream locations: x/L = 0.25, 0.50, 0.75, and 1.0. Compare with Figs. 5 and 6 to see the effect of varying Damköhler number. The solid curve in each of the scatter plots gives the adiabatic, equilibrium temperature distribution.

formulation dictates that $T(\mathbf{x},t) = T^{EQ}(\mathbf{x},t)$, and the computed points naturally fall on the equilibrium $T(\zeta)$ curve. For Cases 2 and 3 the range of temperature values increases for decreasing downstream locations with values increasingly far from the equilibrium curve. Thus for increasing nonequilibrium, whether by moving upstream within the flame or by decreasing the global Damköhler number, temperatures values become subequilibrium and may, for strain rates beyond the extinction limit, obtain free stream values. These represent locations of mixing with no chemical reaction. Due to the steady nature of the SDRL formulation, transient temperature changes due to ignition/extinction effects in the flame can not be addressed. The variation of temperature throughout the flame may be further investigated by examining the mean and rms temperature profiles for a variety of downstream locations. Fig. 8 shows the mean and rms temperature versus normalized radius for the three degrees of nonequilibrium considered at 6 x/L locations: 1.0, 0.75, 0.50, 0.25, 0.15, and 0.05. These show even more clearly the increase in maximum mean and mean centerline temperatures for increasing x/L locations to approximately 3L/4 where the values begin to decrease to the flame tip. The shift in maximum mean temperature from the jet edge to the centerline for increasing downstream locations is also evident. The rms temperature fluctuations increase moving away from the jet centerline and show maxima very near the jet edge for all x/L locations and all degrees of nonequilibrium considered. As the degree of nonequilibrium is increased, rms values at the jet edge in generally increase, and this increase diminishes as the radius approaches the jet centerline.

Figs. 9-11 show the resulting OH mass fraction $Y_{OH}(\mathbf{x},t)$ fields. Notice that the SDRL formulation produces thin layer-like OH fields for the near-equilibrium conditions in Case 1. The OH layer at x/L = 0.25 for these conditions is relatively straight and aligned with the downstream direction and lies well off the jet centerline. Overall, the resulting OH field for Case 1 is strikingly similar to OH PLIF measurements at small x/L locations in turbulent jet diffusion flames under conditions of relatively weak nonequilibrium [22, 23]. By comparison, in Case 2 the strain rates at this location are significantly higher (see Table 1), and the SDRL formulation produces considerably broader and more diffuse structures in the OH mass fraction field with little remaining evidence of the thin layer-like OH zones seen for Case 1. This is also consistent with direct OH PLIF imaging measurements in turbulent jet diffusion flames. For Case 3, the strain rates at x/L = 0.25 are so high that local extinction of the reactions begins to occur where the dissipation rates of Fig. 1 are highest. The remaining OH zones evident in Case 3 are completely broad and distributed and show no remaining evidence of the layer-like structure in the underlying scalar dissipation rate field. A similar transition from thin, layer-like OH mass fraction fields at conditions near chemical equilibrium to broad, distributed OH zones with increasing depth of nonequilibrium can be seen in the results obtained for x/L = 0.50. There again is a striking resemblance of the OH fields that result for each of these three cases with the basic features of OH PLIF images obtained from direct measurements in turbulent jet diffusion flames under conditions of increasing chemical nonequilibrium [22,23]. These similarities to direct OH PLIF imaging measurements in turbulent jet flames are all the more striking in view of the fact that, despite the wide variations in the OH concentration field structure seen in these results with changing downstream position and with increasing depth of nonequilibrium among the three cases considered, all of these fields ultimately resulted from the same conserved scalar data plane shown in Fig. 1. Thus thin "flamelet-like" OH mass fractions at small x/L in Case 1 and the broad "distributed" regions of high OH concentrations in Case 3 all resulted from a simple layer-like structure in the scalar dissipation rate field in Fig. 1 (bottom) and can be reconciled with the single physically-based formulation discussed for these strained dissipation and reaction layers.

The scatter plots for Case 1 (Fig. 9) verify that in the equilibrium limit the SDRL formulation recovers equilibrium OH values for all locations within the flame. For Case 2 (Fig. 10) at x/L locations far downstream all OH mass fraction values are equilibrium or superequilibrium, but at x/L = 0.25 we find a number of subequilibrium values and points of zero OH mass fraction corresponding to locations of local extinction in the flame. The same trends are seen for Case 3, but subequilibrium values and local extinction are found further downstream.

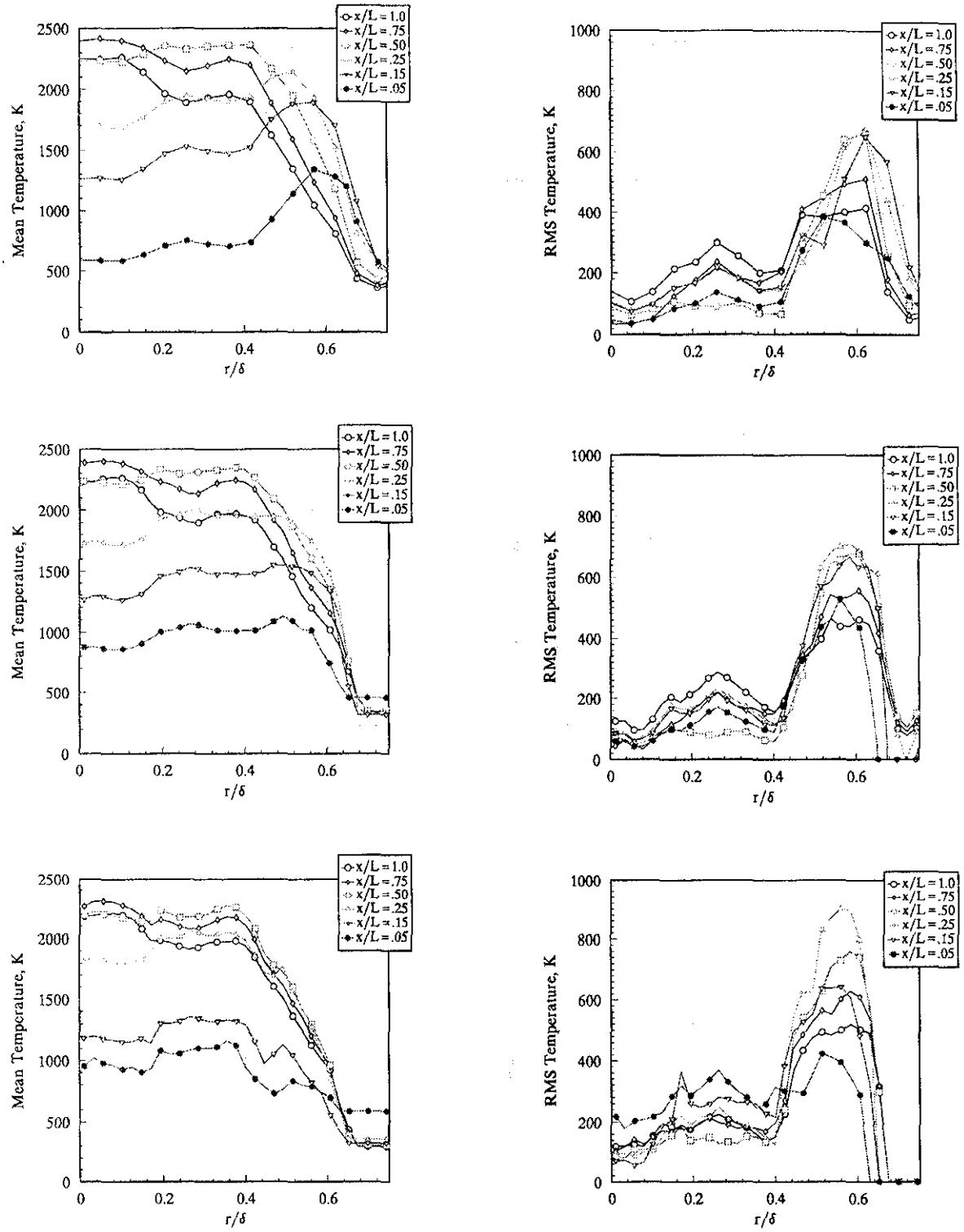

Fig. 8. Radial profiles of mean and rms temperature at 6 downstream locations for the three degrees of nonequilibrium considered. The top figures are for the equilibrium limit (Case 1), middle figures are for moderate nonequilibrium (Case 2), and bottom figures correspond to deep nonequilibrium (Case 3) conditions. The radius is normalized by the local jet diameter, $\delta(x)$.

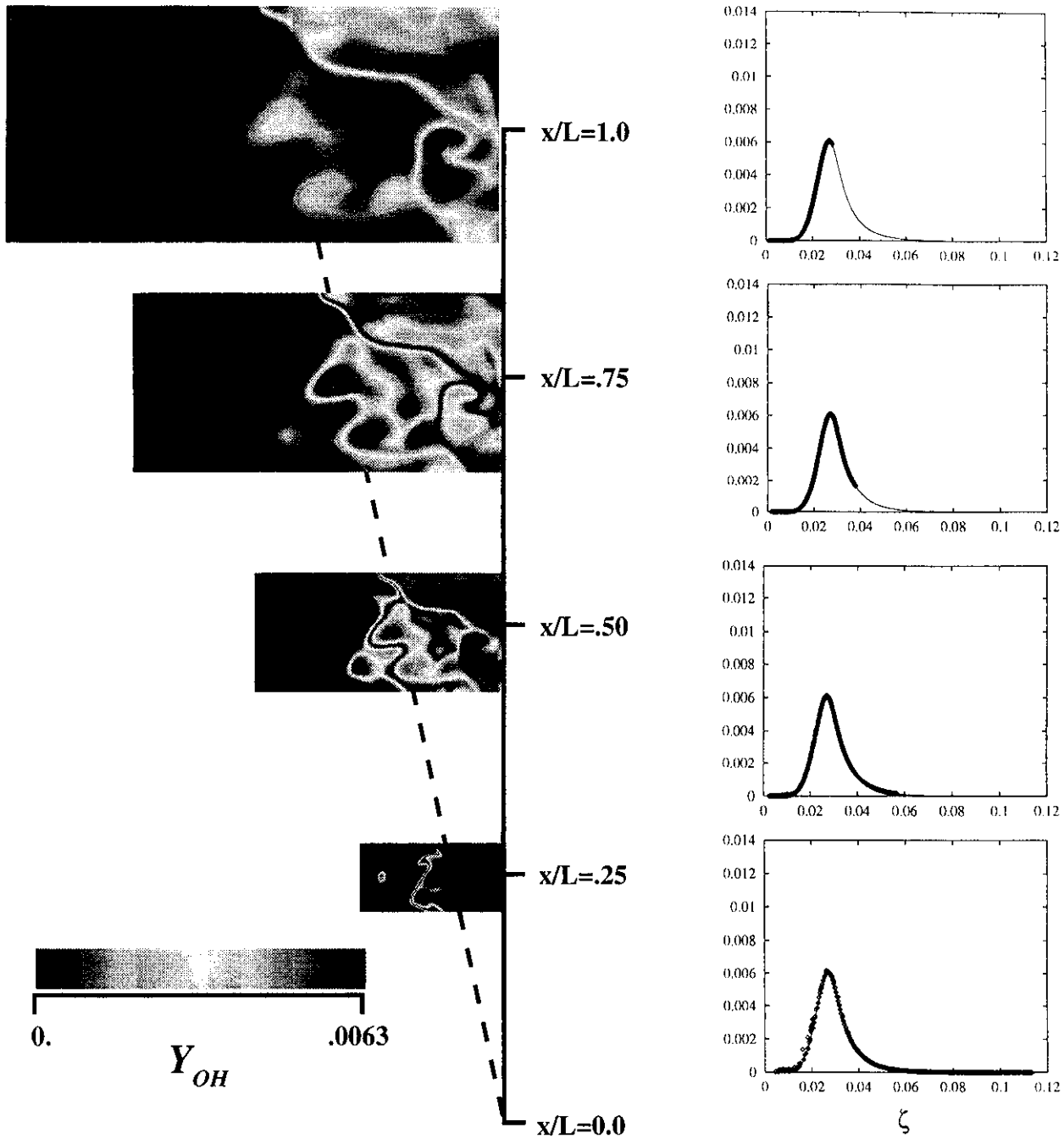

Fig. 9. Strained diffusion and reaction layer (SDRL) model results for composite OH mass fraction fields $Y_{OH}(x,t)$ and the associated scatter plots for a hydrogen-air turbulent jet diffusion flame in the equilibrium limit (Case 1) at four downstream locations: x/L = 0.25, 0.50, 0.75, and 1.0. Compare with Figs. 10 and 11 to see the effect of varying Damköhler number. The solid curve in each of the scatter plots gives the equilibrium OH mass fraction distribution.

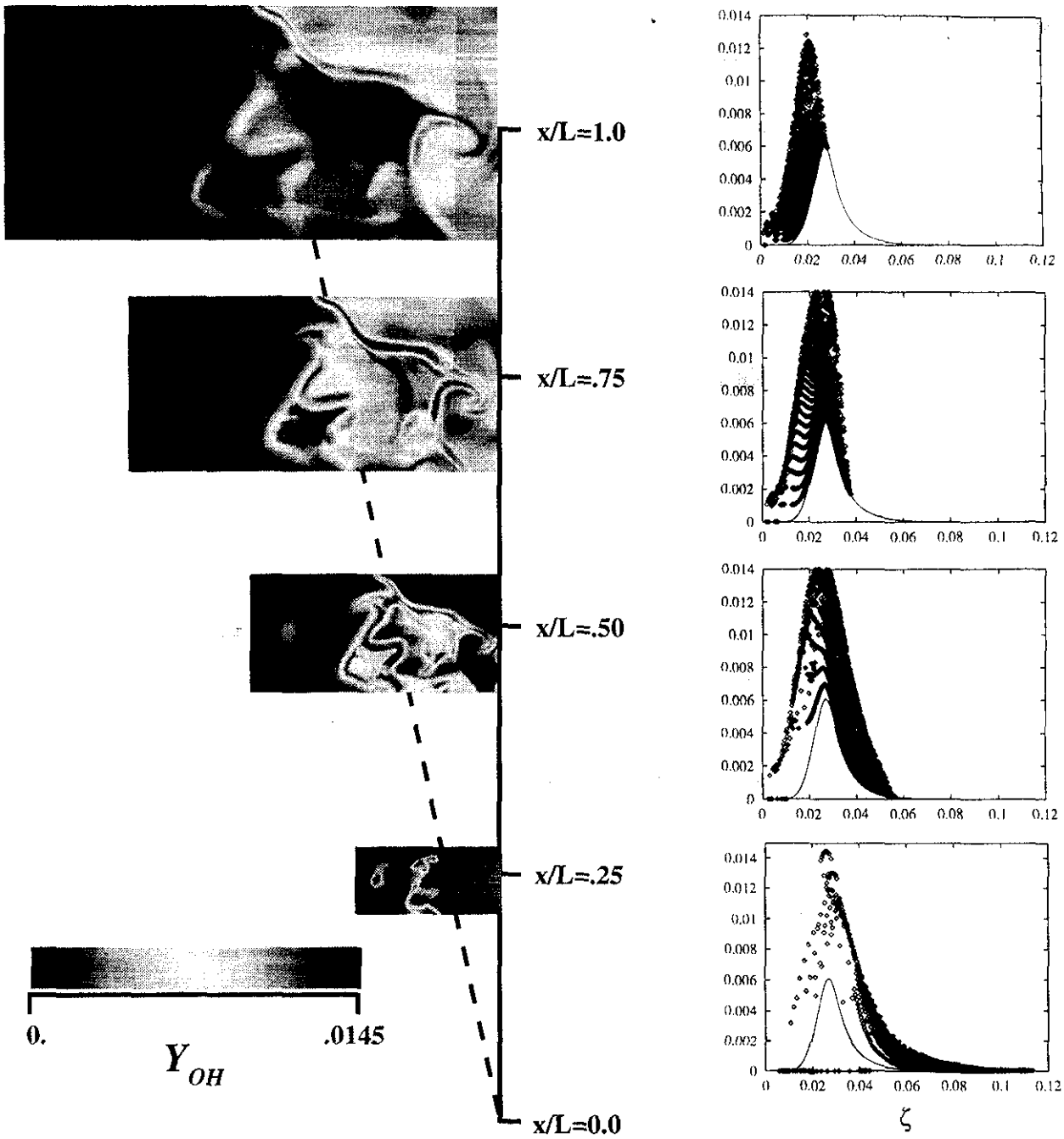

Fig. 10. Strained diffusion and reaction layer (SDRL) model results for composite OH mass fraction fields $Y_{OH}(x,t)$ and the associated scatter plots for a hydrogen-air turbulent jet diffusion flame at moderate nonequilibrium (Case 2) conditions at four downstream locations: $x/L = 0.25, 0.50, 0.75$, and 1.0. Compare with Figs. 9 and 11 to see the effect of varying Damköhler number. The solid curve in each of the scatter plots gives the equilibrium OH mass fraction distribution.

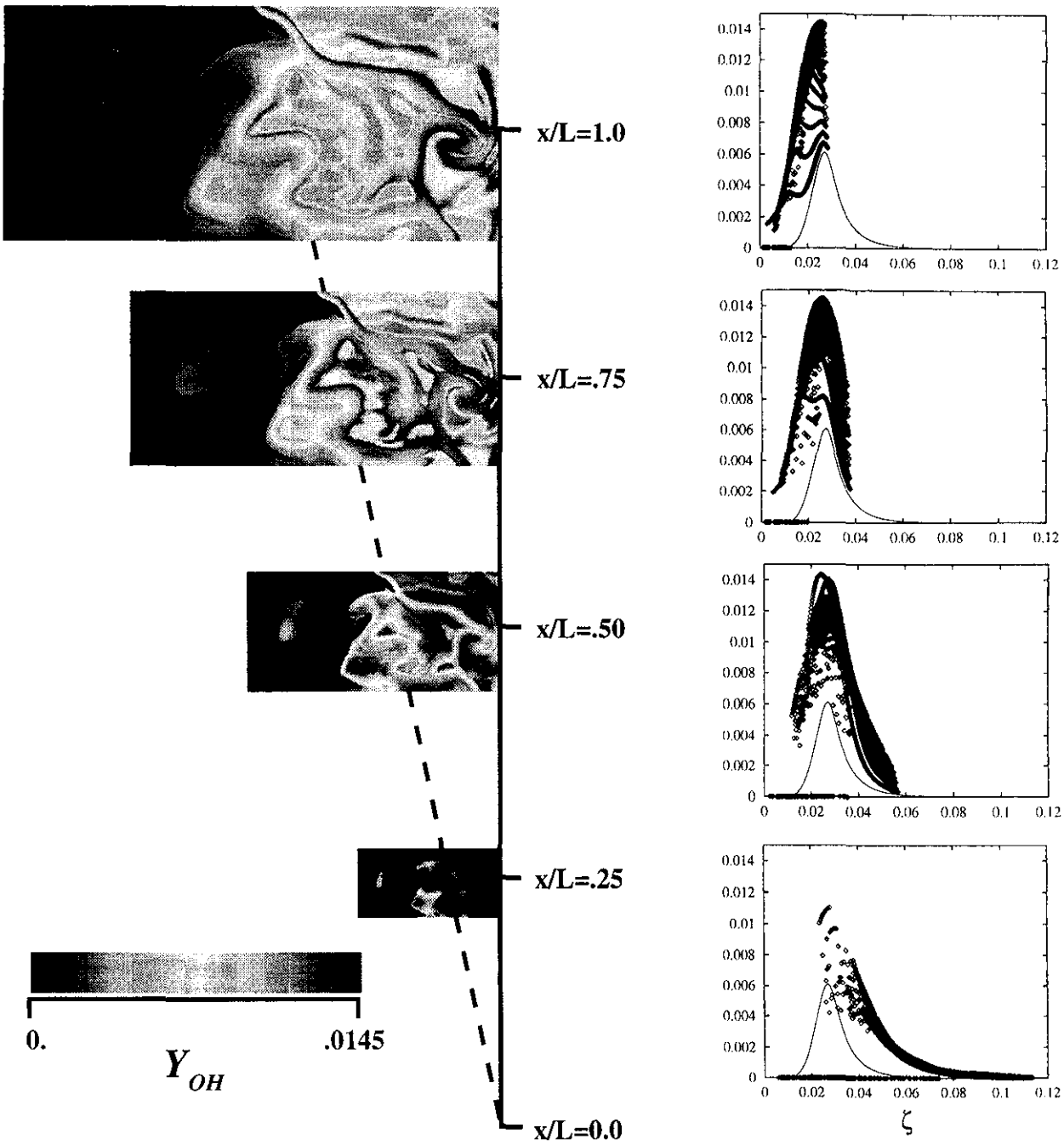

Fig. 11. Strained diffusion and reaction layer (SDRL) model results for composite OH mass fraction fields $Y_{OH}(x,t)$ and the associated scatter plots for a hydrogen-air turbulent jet diffusion flame at deep nonequilibrium (Case 3) conditions at four downstream locations: x/L = 0.25, 0.50, 0.75, and 1.0. Compare with Figs. 9 and 10 to see the effect of varying Damköhler number. The solid curve in each of the scatter plots gives the equilibrium OH mass fraction distribution.

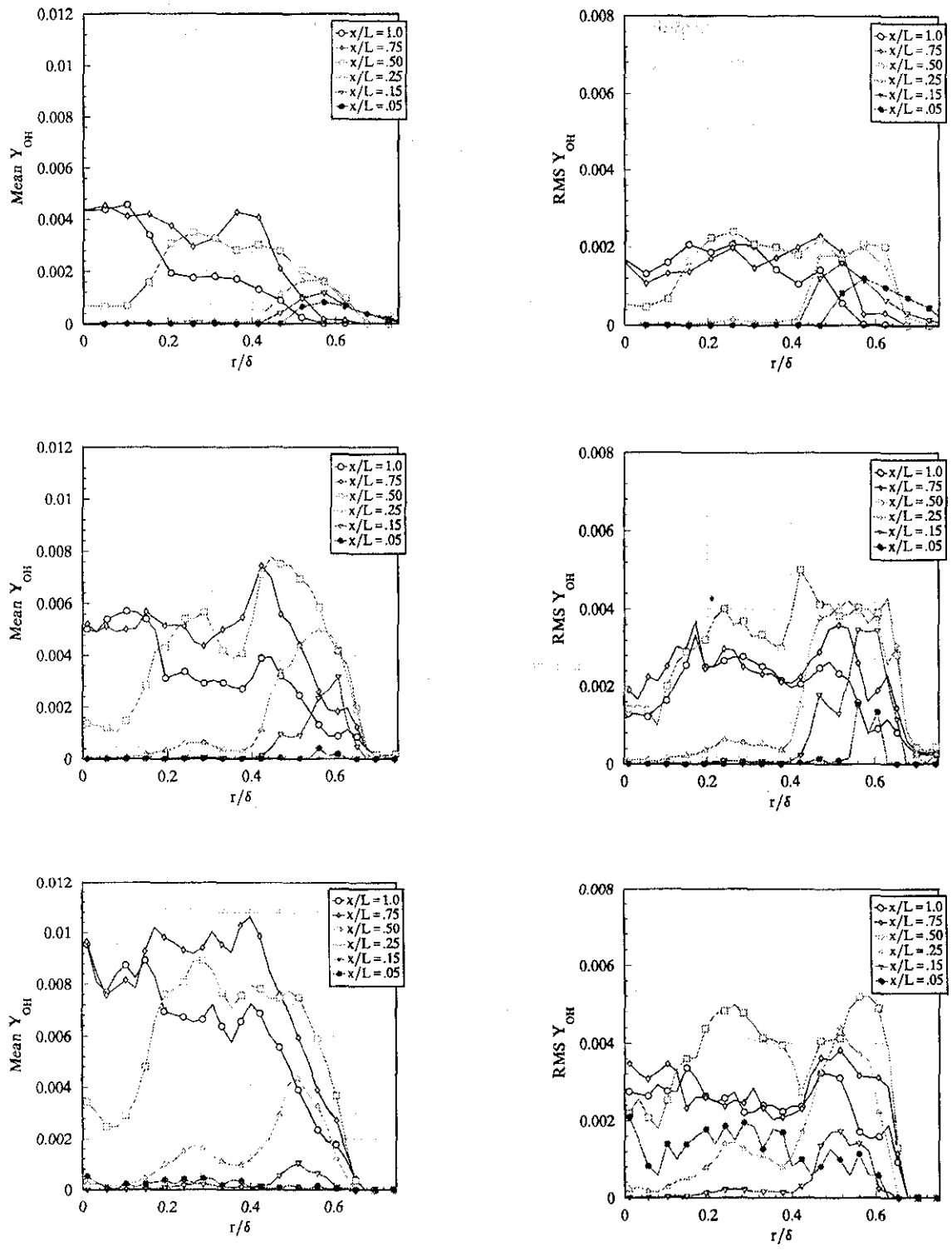

Fig. 12. Radial profiles of mean and rms OH mass fraction at 6 downstream locations for the three degrees of nonequilibrium considered. The top figures are for the equilibrium limit (Case 1), middle figures are for moderate nonequilibrium (Case 2), and bottom figures correspond to deep nonequilibrium (Case 3) conditions. The radius is normalized by the local jet diameter, $\delta(x)$.

Fig. 12 shows the corresponding mean and rms Y_{OH} profiles for the same three degrees of nonequilibrium and 6 downstream locations as used in Fig. 8. Note that a shift in peak mean values occurs for the mean OH mass fraction profiles from the jet edge to the centerline for increasing downstream location similar to that seen for the temperature profiles. In fact there seems to be a relatively strong correlation between the locations of peak mean temperature and OH mass fraction values, especially for moderate to small degrees of nonequilibrium. Peak values for the rms of OH mass fraction fluctuations shift from the jet edge to locations nearer the jet centerline for increasing downstream location in the same manner as the peak mean OH values. There also seems to exist a general increase in rms fluctuations across the width of the flame for increasing degrees of nonequilibrium.

5. Conclusions. The strained dissipation and reaction layer formulation introduced here provides a novel physically-based method for relating the chemical state of nonequilibrium combustion in turbulent flows to the mixing state of conserved scalars. The approach is motivated entirely by the locally one-dimensional dissipation layers seen to result from the dynamics of scalar mixing in turbulent flows. The fact that these dissipation layers are independent of the extent of chemical nonequilibrium in the flow indicates a locally one-dimensional structure in the underlying chemical species fields. The resulting strained dissipation and reaction layer model has certain resemblances to the classical "flamelet" model but is based on entirely different physical observations, derived from entirely different arguments, and limited by an entirely different and more widely applicable set of conditions. Moreover, the local boundary conditions for solution of the local chemical state differ fundamentally from those in flamelet models.

Results obtained when this strained dissipation and reaction layer formulation is applied to imaging measurements of conserved scalar fields in turbulent flows for conditions ranging from near equilibrium to deep nonequilibrium demonstrate characteristics very much like those obtained experimentally in turbulent jet diffusion flames under similar combustion conditions. The temperature fields display a shift in the location of the maximum radial temperature from the jet edge to the centerline for increasing downstream locations and maximum centerline and maximum mean temperatures that occur approximately 3/4 of the flame length downstream. OH mass fraction fields show remarkable resemblances to direct PLIF imaging measurements. Notably, the present SDRL formulation inherently produces results showing a predominance of thin (flamelet) mass fraction layers under conditions of relatively weak chemical nonequilibrium and the natural emergence and dominance of broad (distributed) zones for increasing equilibrium departures. A shift in peak values from the jet edge to the centerline for increasing downstream location occurs for the mean OH mass fraction profiles and is similar to that seen for the temperature profiles. This formulation thus provides a physical and theoretical framework that reconciles these two widely disparate views of the coupling of the underlying fluid dynamics to the reaction chemistry in turbulent combustion within a single model.

Acknowledgements

The authors are grateful to J.-Y. Chen for numerous insightful discussions concerning the 1-D flame code calculations. This work is supported by the Gas Research Institute (GRI) through Contract Nos. 5087-260-1443 and 5088-260-1692, and the Air Force Office of Scientific Research (AFOSR) under Contract No. AFOSR-89-0541. The measurements were conducted with Bob Dibble, Rob Barlow, Dominique Fourquette, and Kenneth Buch in the Combustion Research Laboratories at Sandia National Laboratories (Livermore, CA), which is supported by the Department of Energy, Office of Basic Energy Sciences, Division of Chemical Science. A preliminary version of this paper was presented at the Fall 1993 Meeting of the Western States Section of the Combustion Institute.

References

[1] Dahm, W.J.A. & Buch, K.A. (1991) High resolution, three-dimensional (256^3), spatio-temporal measurements of the conserved scalar field in turbulent shear flows; Turbulent Shear Flows 7, pp. 17-26, W.C. Reynolds, Ed., Springer Verlag, Berlin.

[2] Dahm, W.J.A., Southerland, K.B. & Buch, K.A. (1991) Four-dimensional laser induced fluorescence measurements of conserved scalar mixing in turbulent flows; Applications of Laser Techniques to Fluid Mechanics, pp. 3-18, R. Adrian, Ed., Springer Verlag, Berlin.

[3] Dahm, W.J.A., Southerland, K.B. & Buch, K.A. (1991) Direct, high resolution, four-dimensional measurements of the fine scale structure of $Sc \gg 1$ molecular mixing in turbulent flows; *Phys. Fluids A* **3**, 1115-1127.

[4] Buch, W.J.A. & Dahm, W.J.A. (1992) Fine scale structure of conserved scalar mixing in turbulent shear flows: $Sc \gg 1$, $Sc = 1$ and implications for reacting flows; University of Michigan Report No. 026779-5, The University of Michigan, Ann Arbor, MI.

[5] Buch, K.A., Dahm, W.J.A., Dibble, R.W. & Barlow, R.S. (1992) Equilibrium structure of reaction rate fields in turbulent diffusion flames; *Proc. 24th Symp. (Int'l.) on Comb.* 295-301, The Combustion Institute, Pittsburgh.

[6] Dahm, W.J.A. & Bish, E.S. (1993) High resolution measurements of molecular transport and reaction processes in turbulent combustion; in Turbulence and Molecular Processes in Combustion, pp. 287-302, (T. Takeno, Ed.) Elsevier Science Publishers, Amsterdam.

[7] Siggia, E.D. (1981) Numerical study of small scale intermittency in three-dimensional turbulence; *J. Fluid Mech.* **107**, 375-406.

[8] Kerr, R.M. (1985) Higher-order derivative correlations and the alignment of small scale structures in isotropic numerical turbulence; *J. Fluid Mech.* **153**, 31-58.

[9] Reutsch, G.R. & Maxey, M.R. (1991) Small-scale features of vorticity and passive scalar fields in homogeneous isotropic turbulence; *Phys. Fluids A* **3**, 1587-1597.

[10] Mell, W., Kosály, G. & Riley, J.J. (1993) An investigation of closure models for nonpremixed turbulent reacting flows; AIAA Paper No. 93-0104, AIAA, Washington, D.C.

[11] Montgomery, C.J., Kosály, G. & Riley, J.J. (1993) Direct numerical simulation of turbulent H2-O2 combustion using reduced chemistry; AIAA Paper No. 93-0248, AIAA, Washington, D.C.

[12] Long, M.B. (1993) Proceedings of the 1993 AFOSR Contractors Meeting in Propulsion, AFOSR, Washington, D.C.; also private communication.

[13] Bish, E.S., Dahm, W.J.A., Dowling, D.R. (1993) A strained dissipation and reaction layer formulation for turbulent diffusion flames. Paper No. 93-063, presented at 1993 Fall Meeting, Western States Section / The Combustion Institute, Menlo Park, Ca.

[14] Peters, N. (1984) Laminar diffusion flamelet models in nonpremixed turbulent combustion. *Prog. Energy Combust. Sci.* **10**, 319-339.

[15] Williams, F. A., Combustion Theory, 2nd ed., Addison-Wesley, 1985.

[16] Bilger, R.W. (1988) The structure of turbulent nonpremixed flames. *Proc. 22nd Symp. (Int'l.) on Comb.* 475-488, The Combustion Institute, Pittsburgh.

[17] Chen, J.-Y. (1992) private communication.

[18] Peters, N. (1986) Laminar flamelet concepts in turbulent combustion. *Proc. 21st Symp. (Int'l.) on Comb.* 1231-1250, The Combustion Institute, Pittsburgh.

[19] Becker, H.A., Yamazaki, S. (1978) Entrainment, momentum flux and temperature in vertical free turbulent diffusion flames. *Combustion and Flame*, **33**, 123-149.

[20] Cheng, T.S., Wehrmeyer, J.A., Pitz, R.W. (1992) Simultaneous temperature and multispecies measurement in a lifted hydrogen diffusion flame. *Combustion and Flame*, **91**, 323-345.

[21] Everest, D., Driscoll, J., Dahm, W.J.A., Feikema, D. Images of the 2-D temperature field and temperature gradients to quantify mixing rates within a non-premixed turbulent jet flame. submitted to *Combustion and Flame*, August 1993.

[22] Seitzman, J., Paul, P.H., Hanson, R.K. & Üngüt, A. (1990) AIAA Paper No. 90-0160, American Institute of Aeronautics and Astronautics, Washington, D.C.

[23] Clemens, N.T., P.H. Paul & M.G. Mungal (1992) private communication.